ACCSCIENCE PUBLISHING

International Journal of Bioprinting

RESEARCH ARTICLE

Neural cell responses to spinal implant biomaterials in a 3D-bioprinted cell culture model

David J. Wen[1†], Javad Tavakoli[1,2†*], and Joanne L. Tipper[1,2*]

[1]School of Biomedical Engineering, Faculty of Engineering and Information Technology, University of Technology Sydney, Sydney, Australia

[2]School of Engineering, STEM College, RMIT University, Melbourne, Australia

(This article belongs to the *Special Issue*: *Bioprinting of Nanomaterials for Biomedical Applications*)

Abstract

Spinal implants are vital for treating spinal disorders, yet wear particle-induced complications threaten their long-term success. Despite this, the direct effects of implant-derived particles on neural cells remain largely unexplored, especially given the limitations of conventional 2D culture models to capture such complex interactions. The current study introduces a novel *in vitro* platform consisting of a 3D-bioprinted gelatin methacryloyl (GelMA) hydrogel embedded with neural cells (C6 astrocyte-like and NG108-15 neurons) and spinal implant biomaterial particles, designed to model the spinal cord microenvironment with enhanced physiological relevance. As the first of its kind, this cell-particle-laden system supports the evaluation of neural cell responses to spinal biomaterial particles, including polymers, PEEK-OPTIMA™ and polyethylene Ceridust® 3615, zirconia-toughened alumina (ZTA) ceramic, and CoCrMo metal alloy. The bioprinted platform demonstrated excellent compatibility with various neural cell types and particle compositions, enabling a wide range of biological assays. Cell viability within the 3D model was comparable to traditional 2D cultures, affirming its ability to sustain cell survival while offering improved biomimicry. Biological assays assessing cell viability, reactive oxygen species (ROS) production, and DNA damage provided critical insights into material-specific and time-dependent cellular responses. While no significant cytotoxic effects were observed in short-term cultures, distinct variations in ROS production, and viability emerged based on biomaterial type and exposure duration. Overall, this versatile 3D-bioprinted system presents a robust, scalable tool for mechanistic and toxicological studies of spinal implant wear particles under physiologically relevant conditions.

Keywords: 3D model; Biomaterial particles; Bioprinting; C6 Astrocyte-like cells; Cell viability; Nevural cells; NG108-15 cells; Reactive oxygen species

†These authors contributed equally to this work.

***Corresponding authors:**
Javad Tavakoli
(javad.tavakoli@rmit.edu.au)

Joanne L. Tipper
(joanne.tipper@rmit.edu.au)

Citation: Wen DJ, Tavakoli J, Tipper JL. Neural cell responses to spinal implant biomaterials in a 3D-bioprinted cell culture model. *Int J Bioprint*. 2025;11(4):256-277. doi: 10.36922/IJB025180174

Received: April 29, 2025
Revised: June 4, 2025
Accepted: June 10, 2025
Published online: June 10, 2025

1. Introduction

In the absence of effective tissue engineering strategies to regenerate damaged intervertebral discs, spinal implants remain essential in the treatment of both degenerative and traumatic spinal conditions.[1] These implants are crucial in restoring

stability and functionality to affected regions, offering relief and improving the quality of life for patients.[2,3] Despite their effectiveness, the materials used in spinal implants, including metals, polymers, and ceramics, can generate wear particles over time.[4,5] These particles, particularly in combinations such as metal-on-polymer in total disc replacements, may pose potential risks to surrounding tissues.[6,7] On the other hand, the long-term success of spinal implants is frequently compromised by the generation of wear particles, which can trigger adverse biological responses.[8]

Several studies have analyzed clinical data and examined periprosthetic tissues, revealing a range of detrimental effects associated with spinal implant wear particles.[9–11] These effects include inflammation, hypersensitivity, neurological symptoms, pain, pseudotumor formation, and osteolysis.[12–15] Such responses underscore the importance of understanding the biological impact of wear particles and their potential to disrupt the healing process, as well as overall implant functionality and longevity.[16] Histological analysis of spinal periprosthetic tissues obtained during revision surgery revealed a marked increase in the inflammatory cytokines like tumor necrosis factor-alpha (TNF-α) and interleukin (IL)-6 in regions of inflammation.[17–19] This finding strongly associates stainless steel wear particles with the initiation and continuation of chronic inflammatory responses, highlighting their potential role in long-term complications following spinal implant procedures.[20,21] Both stainless steel and titanium wear debris from spinal instrumentation have been shown to initiate a macrophage-driven inflammatory cascade, resulting in increased local production of TNF-α.[22–24] This cytokine, in turn, drives osteoclastogenesis and promotes apoptosis in nearby cells, contributing to bone resorption and tissue degradation.[21,25]

While clinical studies following revision surgery have highlighted the biological effects of spinal wear particles on periprosthetic tissues, their direct impact on the spinal cord remains largely unexplored. However, recent *in vitro* research has demonstrated that exposure of porcine dural cells and organ cultures to cobalt–chromium–molybdenum (CoCrMo) nanoparticles significantly upregulates the pro-inflammatory chemokine IL-8.[26–28] This increased IL-8 expression compromises endothelial cell integrity, disrupting the blood-spinal cord barrier, and potentially increasing its permeability.[29] These changes could have serious implications for neuroinflammation and the vulnerability of spinal tissues. Furthermore, CoCrMo particle exposure induces substantial structural alterations in the dura mater, including elevated expression of matrix metalloproteinases (MMP-1, MMP-3, MMP-9, and MMP-13), as well as tissue inhibitor of metalloproteinase-1 (TIMP-1).[30] These findings suggest that CoCrMo particles promote tissue remodeling and the loosening of collagen fibers, which could facilitate the penetration of nanoparticles into the dura mater and possibly the spinal cord.[7] Evidence also showed that *in vivo* epidurally introduced particles can penetrate both the dural barrier and the blood-spinal cord barrier, potentially allowing migration into deeper neural structures. Additionally, the rapid circulation of cerebrospinal fluid from the subarachnoid space into the spinal canal—especially through perivascular pathways—may further enhance nanoparticle transport and infiltration into spinal tissues, raising concerns about their potential neurotoxic effects.[31,32] Motivated by these findings, an *in vitro* study using CoCr and stainless-steel wear particles demonstrated that CoCr particles significantly reduced glial cell viability and induced DNA damage in both astrocytes and microglial cells.[26] Notably, CoCr particles also caused a dose-dependent increase in glial fibrillary acidic protein (GFAP) expression, indicating astrocyte activation. In contrast, while stainless steel wear particles induced DNA damage in both glial and astrocyte cells, their impact on glial cell viability was minimal, with only the ions released from stainless steel causing a significant decline in glial cell viability.

To the best of our knowledge, only a limited number of studies have investigated the biological impacts of metallic wear particles and the potential neurotoxic effects of wear debris from different material types remain largely unexplored. To address this gap, the current study employs a 3D-bioprinted neural cell culture model based on gelatin methacryloyl (GelMA) hydrogels to evaluate the biological effects of ceramic, polymer, and metal wear particles. This advanced *in vitro* model more accurately mimics the cellular and extracellular matrix interactions observed *in vivo*, providing a more physiologically relevant test system than traditional 2D cell cultures. As such, it allows for a controlled investigation into cell viability, oxidative stress responses, and potential DNA damage induced by wear particles from varying material compositions.

Understanding the impact of wear particles on neural cells is crucial for advancing spinal implant design, optimizing biomaterial selection, and minimizing the neurotoxic risks associated with implant degradation. The insights gained from this study could play a pivotal role in developing neuroprotective strategies for spinal surgery, while also contributing to the improvement of long-term implant biocompatibility. By addressing these factors, the findings could help enhance patient outcomes and extend the functional lifespan of spinal implants.

2. Materials and methods

2.1. Cell culture preparation

2.1.1. Neural cell lines and cell culture media

C6 astrocyte-like (rat glioma) and NG108-15 (derived from mouse neuroblastoma fused with rat glioma) cell lines were obtained from the American Tissue Culture Collection (ATCC) and the European Collection of Cell Culture (ECACC), respectively. The cell culture medium for C6 astrocyte-like cells consisted of Ham's F-12 nutrient mix (Sigma-Aldrich, Germany) supplemented with 10% (v/v) fetal bovine serum (FBS) (Bovogen, Australia). For NG108-15 cells, the cryopreservation medium comprised Dulbecco's Modified Eagle's Medium (DMEM; Gibco, USA) supplemented with 20% (v/v) FBS and 10% (v/v) dimethyl sulfoxide (DMSO; Sigma-Aldrich). For cell culture, the cryopreservation medium was further supplemented with 100 U/mL penicillin (Gibco) and 100 μg/mL streptomycin (Gibco).

2.1.2. Cell culture

Cell passaging was performed when cultures reached approximately 70–80% confluence. Before passaging, a complete cell culture medium and trypsin (Gibco) were pre-warmed to 37°C in a water bath (Thermoline Scientific, Australia). The existing medium in the culture flask was aspirated, and the cells were washed with Dulbecco's Phosphate Buffered Saline solution (PBS; Sigma-Aldrich). Subsequently, 0.25% (v/v) trypsin-EDTA (Gibco) was added (1 mL for a T25 flask and 3 mL for a T75 flask), and the flasks were incubated at 37°C with 5% CO_2 for 3 min. An equal volume of complete medium was then added to neutralize the trypsin. The cell suspension was transferred to a 15 mL centrifuge tube and centrifuged (Thermoline Scientific) at 300 × *g* for 5 min. Following centrifugation, the supernatant was aspirated and the cells were then transferred into new culture flasks containing fresh medium and maintained at 37°C with 5% CO_2 (Heracell™ VIOS 160i, Thermo Fisher Scientific, USA). Cell culture was conducted both in isolation and co-culture conditions. When required, cell counting was performed using a hemocytometer and the trypan blue (Sigma-Aldrich) exclusion assay.

2.2. Particles

2.2.1. Particle types

This study utilized a variety of particulate materials, encompassing polymers, metals, and ceramics. The polymer particles included polyetheretherketone (PEEK-OPTIMA™; from Invibio Biomaterial Solutions, UK) and polyethylene (Ceridust® 3615; from Hoechst, Germany). The ceramic particles were composed of zirconia-toughened alumina (ZTA; Inframat Advanced Materials, USA), while the metallic particles were made from a cobalt–chromium–molybdenum (CoCrMo) alloy (American Elements, USA). These materials were selected to represent common biomaterials used in spinal implants, providing a comprehensive analysis of the biological impact of wear debris from diverse material types.

2.2.2. Particle preparation and separation

Sequential filtration was performed to separate particles by size using 25 mm polycarbonate membrane filters (8, 0.8, and 0.1 μm pore sizes; Whatman). Membrane filters were sterilized by washing with 70% (v/v) ethanol, rinsing with deionized water, air-drying at room temperature, and exposing them to ultraviolet (UV) light for 30 min. A 100 mg particle sample was suspended in 20 mL of distilled water in a 50 mL centrifuge tube and then sonicated (Unisonics Australia) for 40 min to ensure uniform dispersion (5 g/L concentration). Immediately after sonication, the suspension was filtered through the membranes. The filters were carefully transferred to sterile Petri dishes using tweezers and dried in an oven (Skope, New Zealand) at 50°C for at least 30 min. The size-separated particles were then subjected to scanning electron microscopy (SEM; Zeiss; EVO LS 15) characterization and cell culture experiments.

2.2.3. Scanning electron microscopy imaging

Dried filters were directly coated with a 3 nm layer of gold/palladium or carbon using a sputter coater before SEM imaging. PEEK-OPTIMA™, Ceridust® 3615, and ZTA samples were coated with gold/palladium, while CoCrMo samples were coated with carbon. Imaging was performed at 5 kV or 10 kV with a working distance of 4.9–21 mm. Four magnifications (100×, 400×, 700×, and 1500×) were used, with at least three images captured per magnification for each filter and material.

2.2.4. Particle characterization

The SEM images were analyzed using ImageJ open-source software (Open-source image processing software developed by the National Institutes of Health [NIH] in the USA) to measure particle size, area distribution, and morphology. Measurements included particle area, perimeter, length (Feret's diameter along the major axis), and width (Feret's diameter along the minor axis). Particles were categorized into size ranges: <0.1, 0.1–0.8, 1.0–8, and >8 μm. Additionally, the particle count per image area (N/A) and the average particle area within each size range (P/N) were calculated. A minimum of 100 particles per material were manually measured by outlining each particle. To minimize human error, overlapping or agglomerated particles were excluded from the analysis.

2.3. Development of 3D model using bioprinting

2.3.1. Preparation of GelMA hydrogel

GelMA (CELLINK, Sweden) hydrogel solution was prepared using the CELLINK GelMA Kit, which included GelMA powder and the photoinitiator lithium phenyl-2,4,6-trimethylbenzoylphosphinate (LAP; CELLINK). LAP was dissolved in PBS and mixed at 60°C for 20 min to achieve a 0.25% (w/v) solution, which was then filter-sterilized (0.22 μm) in a class II biosafety cabinet (Thermoline Scientific). The sterilized LAP/PBS solution was subsequently added to GelMA powder and mixed at 50°C for 20 min to obtain a 5% (w/v) GelMA solution. The 5% (w/v) GelMA concentration was selected based on our previous findings, which identified this formulation as optimal for supporting the viability of neuronal and astrocyte-like cells over a 7-day culture period under standard conditions.[33]

2.3.2. Preparation of cell-laden GelMA hydrogel

Neural cells (C6 astrocyte-like and NG108-15) were cultured separately at 37°C with 5% (v/v) CO_2 until reaching 80% confluence (as explained in **Section 2.1**). The culture medium was then removed, and trypsin was added for 3 min to detach the cells. An equal volume of culture medium was used to neutralize the trypsin, and the cell suspension was transferred to a 15 mL Falcon tube for centrifugation at 300 × *g* for 5 min. The supernatant was carefully aspirated, and the resulting cell pellet was resuspended in fresh culture medium (as explained in **Section 2.1**) to achieve a final concentration of 1×10^4 cells/mL. Subsequently, 100 μL of this cell suspension was added to 1 mL of GelMA hydrogel solution. The mixture was thoroughly homogenized by gentle aspiration in a 15 mL centrifuge tube to ensure uniform cell distribution within the cell-laden GelMA hydrogel.

2.3.3. Preparation of cell-laden GelMA hydrogel embedded with particles

Particle stock solutions were first prepared in cell culture media at a concentration of 1 mg/mL. Added to 100 μL of cell suspension (1×10^4 cells/mL) were 1.3 μL of PEEK-OPTIMA™, 1 μL of Ceridust® 3615, 2.5 μL of ZTA, and 4.2 μL of CoCrMo (Table 1) to achieve the desired specific particle volumes (μm³/cell). PEEK-OPTIMA™ and Ceridust® 3615 3D model particles were incorporated at a concentration of 100 μm³ per cell, whereas ZTA and CoCrMo model particles were introduced at 50 μm³ per cell. Additionally, CoCrMo model particles were prepared at two additional concentrations—0.5 and 5 μm³ per cell—to assess dose-dependent effects. The final cell/particle suspensions were mixed with 1 mL of GelMA hydrogel. These dosing strategies were informed by previous 2D *in vitro* studies in the existing literature.[26,34,35]

2.3.4. Bioprinting of 3D droplet hydrogels

The resulting GelMA hydrogel solutions were then loaded into a 3 mL cartridge for 3D bioprinting. After securely attaching the nozzle to the cartridge, the assembly was placed into the temperature-controlled print head of the bioprinter (CELLINK BIO X6). The bioprinting parameters, including extrusion pressure, printing speed, and temperature, were subsequently optimized to fabricate simple droplet hydrogels within the well plates. Finally, the printed hydrogels were photocrosslinked by exposure to UV light at 365 nm with an intensity of 19.42 mW/cm² for 120 s. The bioprinted cell-laden GelMA droplets (with or without model particles) were cultured, as explained in **Section 2.1**.

2.4. Three-dimensional biological assessments

2.4.1. Three-dimensional cell viability assay

GelMA hydrogel droplets were bioprinted into 48-well plates and cultured at 37°C and 5% (v/v) CO_2 for 5 days. A luminescent ATP detection assay kit (CellTiter-Glo 3D Cell Viability Assay Kit; Promega, USA), consisting of two fluorescent dyes, namely a green fluorescent calcein AM dye (for live cells; Invitrogen, USA) and an ethidium homodimer-1 dye (for dead cells; Invitrogen), was used to evaluate cell viability on Days 1, 3, and 5. In addition, the DNA of cells was stained with a blue-fluorescent Hoechst 33342 dye (Life Technologies, USA). Briefly, 50 μL of lysis buffer was added to each well to facilitate cell membrane

Table 1. Particle mass to prepare suspensions with desired concentrations

Particle	Volume (μm³)	Density (g/cm³)	Mass (μg per cell)	Cell number (per droplet)	Particle mass (μg per droplet)
PEEK-OPTIMA™	100	1.3	1.3×10^{-4}	1×10^4	1.3
Ceridust® 3615	100	1	1×10^{-4}	1×10^4	1
ZTA	50	5	2.5×10^{-4}	1×10^4	2.5
CoCrMo	50	8.4	4.2×10^{-4}	1×10^4	4.2

Abbreviations: CoCrMo, cobalt–chromium–molybdenum; PEEK, polyetheretherketone; ZTA, zirconia-toughened alumina.

disruption and ATP stabilization. The plate was then shaken for 5 min at 50 × *g*. Following cell lysis, 50 µL of luminescent substrate solution was added to each well. The plate was shaken again under the same conditions for an additional 5 min to ensure proper mixing and reaction initiation. Subsequently, the plate was incubated in the dark at room temperature for 10 min to allow the luminescent signal to stabilize. Luminescence, which is directly proportional to the intracellular ATP content and hence viable cell number, was then measured using a microplate reader (Varioskan LUX, Thermo Scientific). For qualitative analysis, GelMA droplet hydrogels were imaged immediately using a confocal EVOS M5000 microscope at 10× magnification with green fluorescent protein (GFP; emission: 525/50 nm), red fluorescent protein (RFP; emission: 593/40 nm), and 4',6-diamidino-2-phenylindole (DAPI; emission: 447/60 nm) emission filters for calcein AM, ethidium homodimer-1, and Hoechst 33342 stains, respectively. Three replicates of GelMA droplets were bioprinted for each particle type and a total of three images were taken for each droplet. In addition, a negative control of cell only and a positive control of 5% (v/v) DMSO was utilized, and a particle-only control was also used to ensure that particles did not interfere with the luminescent readings for this assay.

2.4.2. Reactive oxygen species detection assay

The DCFDA - Cellular ROS Assay Kit (Abcam, UK) was used to measure the production of reactive oxygen species (ROS) by cells in different particle model bioprinted droplets. The cell culture media was aspirated from each well, and bioprinted droplets were washed with ROS assay buffer. The cells were stained with 100 µL diluted DCFDA (2′,7′-dichlorofluorescin diacetate; a cell-permeant reagent) solution and incubated at 37°C and 5% (v/v) CO_2 for 45 min. The positive control was established by using 100 µL of 200 µM hydrogen peroxide, followed by a 2-h incubation (96 well plate). Subsequently, fluorescence was measured with a plate reader at excitation and emission of 485 and 535 nm, respectively.

2.4.3. DNA damage

To evaluate the impact of model wear particles on DNA integrity in C6 astrocyte-like cells, γ-H2AX foci formation—a marker of DNA double-strand breaks—was assessed at multiple time points (1, 2, and 4 h post-exposure). For immunofluorescent detection, bioprinted droplets were first washed with PBS and permeabilized with 100 µL of 0.5% Triton X-100 solution for 3 min at room temperature. The droplets were then washed twice with PBS, followed by the addition of 50 µL of primary antibody solution targeting γ-H2AX (Abcam). Samples were incubated at 37°C in a humidified atmosphere with 5% CO_2 for approximately 45 min. After incubation, the droplets were washed again with PBS, and 50 µL of a fluorescently labeled secondary antibody was added, followed by a 25-min incubation under the same conditions. After a final PBS wash, mounting medium containing Hoechst dye was applied to stain cell nuclei. The droplets were then imaged using a fluorescence microscope to quantify γ-H2AX foci formation.

2.5. Biological assessments in 2D

To assess cell viability in 2D culture, a luminescent ATP assay kit (Abcam) was used. Briefly, before conducting the luminescent ATP detection assay, cells were seeded into 96-well plates. Fifty microliter of lysis buffer was added to each well to facilitate cell membrane disruption and ATP stabilization. The plate was then shaken for 5 min at 50 × *g*. Following cell lysis, 50 µL of luminescent substrate solution was added to each well. The plate was shaken again under the same conditions for an additional 5 min to ensure proper mixing and reaction initiation. Subsequently, the plate was incubated in the dark at room temperature for 10 min to allow the luminescent signal to stabilize. Luminescence, which is directly proportional to the intracellular ATP content and hence viable cell number, was then measured using a microplate reader (Days 1, 3, and 7). Fluorescence microscopy (DP80 and Nikon ECLIPSE Ti2, Japan) was utilized for imaging fluorescently stained cells for qualitative analysis of cell viability. An inverted microscope (Olympus CKX53, Japan) was used for bright-field microscopy.

2.6. Statistical analysis

Statistical analysis was performed using the SPSS software, v22.0 (IBM Corp., Armonk, NY, USA). Two-way analysis of variance (ANOVA) was utilized to assess cell viability and ROS levels between 3D model particles. Fixed factors included cell culture time points and biomaterial types, analyzed with statistical significance of 0.05. Post-hoc multiple comparisons were conducted using a Bonferroni adjustment. All experiments included at least three biological replicates. In addition, statistical significance was analyzed within 3D model particles using one-way ANOVA tests. For proportional or percentage data that does not follow a binomial distribution, an arcsine transformation was used to help normalize the distribution of data.

3. Results

3.1. Particle characterization

This study utilized particles from various materials, including PEEK-OPTIMA™, Ceridust® 3615, ZTA, and CoCrMo alloy. Particle characterization involved size distribution analysis and morphological assessment

(Figure 1). Sequential filtration using polycarbonate membrane filters (8, 0.8, and 0.1 μm pore sizes) categorized particles into >8, 0.8–8, and 0.1–0.8 μm size ranges. SEM analysis revealed that PEEK-OPTIMA™ particles exhibited a granular or irregular morphology across all size ranges (Figure 1), with a mean diameter of 7.6 ± 3.9 μm and a size range of 0.54–83.2 μm. While 95% of particles were <8 μm, 43% were in the submicron range. Larger particles (>8 μm) accounted for ~50% of the total particle area (Figure 2a). Ceridust® 3615 particles displayed a granular and polygonal morphology (Figure 1), with a mean diameter of 6.4 ± 2.7 μm and a size range of 0.49–22.1 μm. Approximately, 92.3% of particles were <8 μm, with a notable proportion (1%) in the 0.1–0.8 μm range (Figure 2b).

Similarly, ZTA particles exhibited granular and polygonal morphology (Figure 1), with a mean diameter of 3.7 ± 3.5 μm and a size range of 0.45–20.3 μm. Most particles (99%) were <8 μm, with 73% in the 0.8–8.0 μm range. Additionally, 99.5% of the total particle area was within this range (Figure 2c). In contrast, CoCrMo particles were primarily globular, with some polygonal shapes (Figure 1). Their mean diameter was 5.9 ± 1.2 μm, within a size range of 2.1–11.6 μm. Most particles (88%) were <8 μm, with 88.5% falling in the 0.8–8.0 μm range. However, while 11.5% of particles were >8 μm, they contributed to 56.2% of the total particle area (Figure 2b).

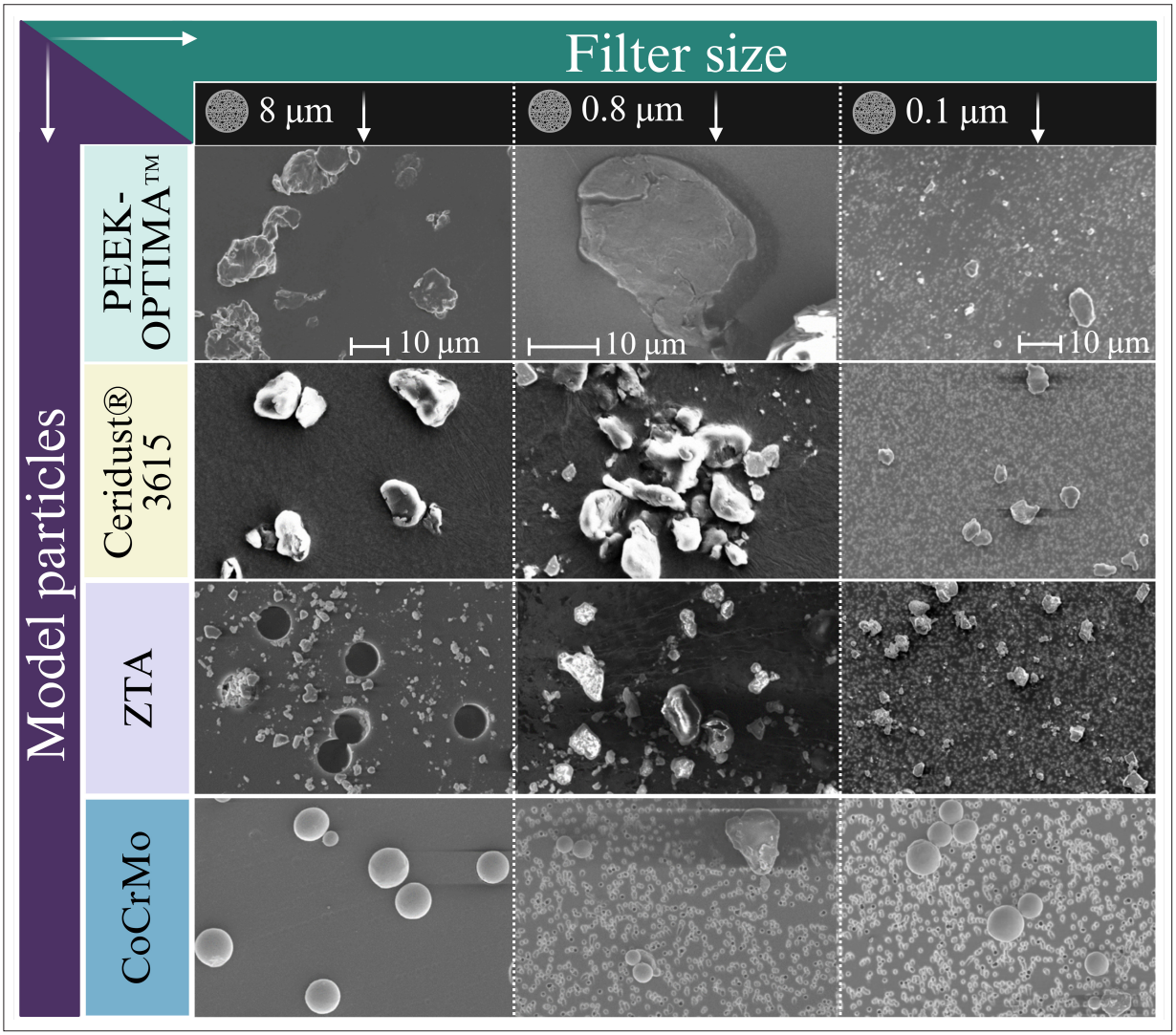

Figure 1. SEM images of model particles, including aggregates and microsized particles, collected using 8, 0.8, and 0.1 μm filters. A consistent scale bar of 10 μm was applied across all SEM images (each filter size) for uniform comparison. Abbreviations: CoCrMo: Cobalt–chromium–molybdenum; PEEK: Polyetheretherketone; SEM: Scanning electron microscopy; ZTA: Zirconia-toughened alumina.

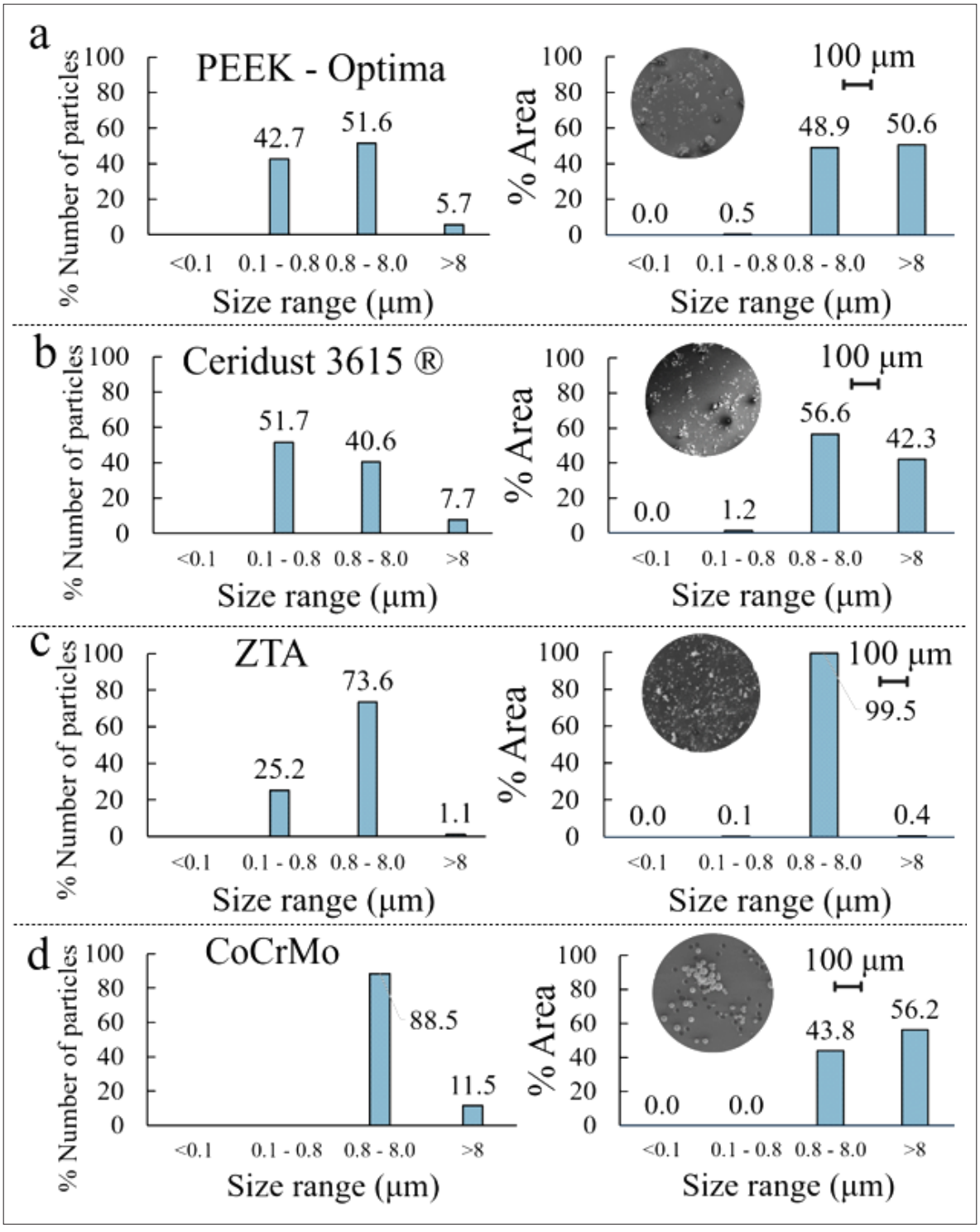

Figure 2. The percentage frequency and area distribution of various model particles determined from the SEM images, as a function of particle size: (a) PEEK-OPTIMA™, (b) Ceridust® 3615, (c) ZTA, and (d) CoCrMo. Abbreviations: CoCrMo: Cobalt–chromium–molybdenum; PEEK: Polyetheretherketone; SEM: Scanning electron microscopy; ZTA: Zirconia-toughened alumina.

3.2. Optimization of 3D bioprinting process and cell viability

In this study, extrusion pressure was the primary variable parameter, while bed temperature, print head temperature, and print speed were maintained at constant values of 10°C, 24°C, and 11 mm/s, respectively. Our findings indicate that an extrusion pressure of 6 kPa facilitated the generation of consistent GelMA droplets with satisfactory structural integrity (Figure 3a and b). Furthermore, the effect of four distinct nozzle gauge sizes—20G, 22G, 25G, and 27G—was evaluated for the droplet printing of GelMA hydrogels mixed with particles. The print speed and extrusion pressure were fixed at 11 mm/s and 6 kPa, respectively. Nozzles with gauge sizes of 20G (0.58 mm inner diameter) and 22G (0.41 mm inner diameter) successfully extruded the GelMA hydrogel–particle mixture. Conversely, nozzles with gauge sizes of 25G (0.25 mm inner diameter) and 27G (0.20 mm inner diameter) failed to achieve consistent extrusion of the bioink–particle mixture. Based on these observations, the 22G nozzle was selected for the fabrication of 3D model particle constructs, both with and without the incorporation of neural cells (Figure 3c).

To assess the biocompatibility and proliferation potential of neural cells within the 3D-bioprinted environment, cell viability was evaluated at Days 1, 3, and 7 within 5% (w/v) GelMA hydrogels and compared to 2D cell culture models as a control (Figure 3d and e). Both C6 Astrocyte-like and NG108-15 cells were seeded at an initial concentration of 1×10^4 cells/mL across both 2D and 3D models (Figure 3f). A progressive increase in cell viability was observed from Day 1 to Day 7 in both environments. Notably, the proliferation rates of cells within the GelMA hydrogels were comparable to those in the 2D control (Figure 3d and e). Qualitative analysis further confirmed enhanced proliferation over the 7 days of cell culture. By Day 7, NG108-15 cells exhibited neurite outgrowth, indicating that the bioprinted 3D droplets supported the growth of these cells. The incidence of cell death remained minimal throughout the 7-day culture period, as evidenced by the sparse presence of red dots from propidium iodine staining.

3.3. Biological assessments

3.3.1. Cell viability

The viability of C6 astrocyte-like and NG108-15 cells was assessed over a 5-day culture period in both experimental groups (cells embedded with model particles in 3D-bioprinted hydrogels) and control groups (cells embedded without particles) (Figure 4). Luminescence readings, indicative of cellular metabolic activity, showed a continuous increase in viability for C6 astrocyte-like cells across the 5 days (Figure 4a). A comparable trend was observed for NG108-15 cells; however, a slight decline in viability was noted on Day 5 compared to Day 3, suggesting a potential sensitivity to prolonged culture conditions or particle exposure (Figure 4b).

Our statistical analysis, conducted using separate one-way ANOVA tests, indicated that the viability of C6 astrocyte-like cells showed no significant differences between the control group (cells-only embedded in 3D-bioprinted hydrogels) and our embedded model particles in 3D-bioprinted hydrogels: CrCoMo (p = 0.65), ZTA (p = 0.34), PEEK-OPTIMA™ (p = 0.058), and Ceridust® 3615 (p = 0.94). Comparable results were observed for NG108-15 cells. Our statistical analysis revealed no significant differences in NG108-15 cell viability between the control group (cells-only in 3D-printed hydrogels) and cell exposed to model particles in 3D-bioprinted hydrogels: CrCoMo (p = 0.32), ZTA (p = 0.83), PEEK-OPTIMA™ (p = 0.64), and Ceridust® 3615 (p = 0.56). Additionally, there were no significant variations in the viability of C6 astrocyte-like and NG108-15 cells across different particle volumes (0.5, 5, and 50 μm³ per cell) within the CrCoMo model particle (p < 0.46). However, for both cell types, a significant revduction in viability (p < 0.05) was observed in the positive control (cells exposed to DMSO) at each time point when compared to the cell-only negative control.

We performed a two-way ANOVA statistical analysis to assess the impact of culture time, biomaterial type, and their interaction on the viability of C6 astrocyte-like cells. The assessment was based on estimated marginal mean luminescent values (±95% confidence interval [CI]) obtained from an ATP assay, which served as an indicator of cell viability (Figure 5). These values were measured for C6 astrocyte-like cells exposed to different model particles or at different dose concentrations over time (Table 2).

Our statistical analysis demonstrated a significant interaction between culture time and biomaterial type (p < 0.001, Figure 5a). Additionally, both culture time and biomaterial type had a significant impact on the viability of C6 astrocyte-like cells (p < 0.001, Figure 5b and c). The post hoc analysis further revealed significant differences in cell viability across the culture time points (Days 1, 3, and 5), with a progressive increase from Day 1 to Day 3, which continued through Day 5 (Figure 5b).

We observed no significant difference in cell viability (p < 0.9) for CoCrMo model particles across varying volumes (0.5, 5, and 50 μm³ per cell, Tables 1 and 2). However, the overall cell viability was significantly higher for CoCrMo (50 μm³ per cell) compared to PEEK-OPTIMA™, Ceridust® 3615, and ZTA model particles (p < 0.001). No significant differences in cell viability were found between PEEK-OPTIMA™ and Ceridust® (p = 0.6) or between

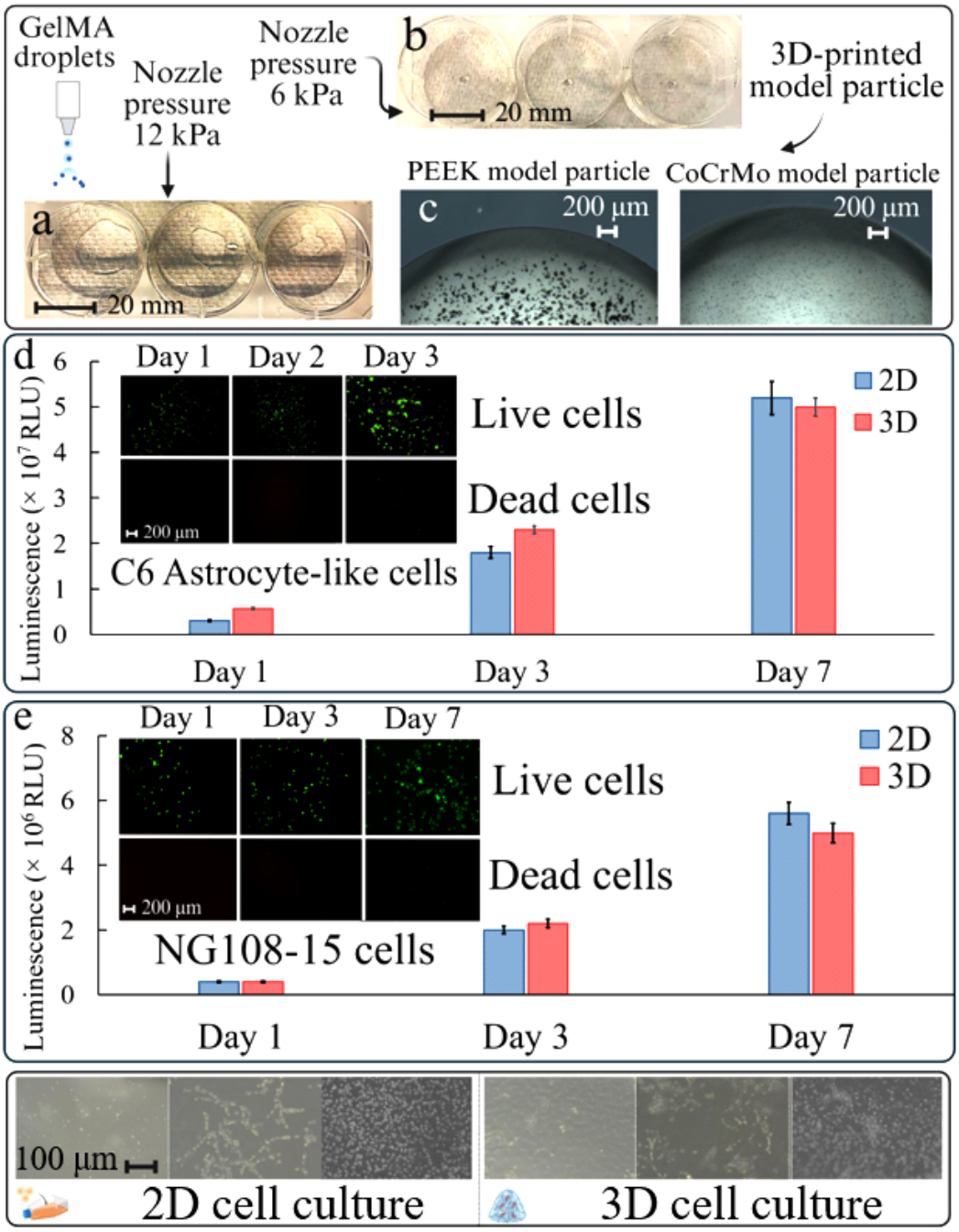

Figure 3. Photographic images of 3D-bioprinted droplet GelMA hydrogels with 5% (w/v) concentration using a BIO X6 bioprinter at 12 kPa (a) and 6 kPa (b). (c) Microscopic images of bioprinted 5% (w/v) GelMA hydrogel droplets, embedded with PEEK-OPTIMA™ (100 µm³ per cell, left) and CoCrMo (50 µm³ per cell, right) particles. The printing parameters of nozzle temperature, extrusion pressure, and speed were 24°C, 6 kPa, and 11 mm/s, respectively. Qualitative and quantitative analyses of cell viability in 3D models for C6 astrocyte-like (d) and NG108-15 cells (e) compared to 2D cell culture models (control), including fluorescence microscopy images of cells in 3D-bioprinted GelMA (5% w/v). (f) Bright-field microscope images of C6 astrocyte-like cells in 2D cell culture (top) compared to C6 astrocyte-like cells in 3D GelMA hydrogels (bottom) at Days 1, 3, and 7 (cell density for 2D and 3D cell culture models = 1×10^4 cells/mL). Abbreviations: CoCrMo: Cobalt–chromium–molybdenum; GelMA: Gelatin methacryloyl; PEEK: Polyetheretherketone; SEM: Scanning electron microscopy; ZTA: Zirconia-toughened alumina.

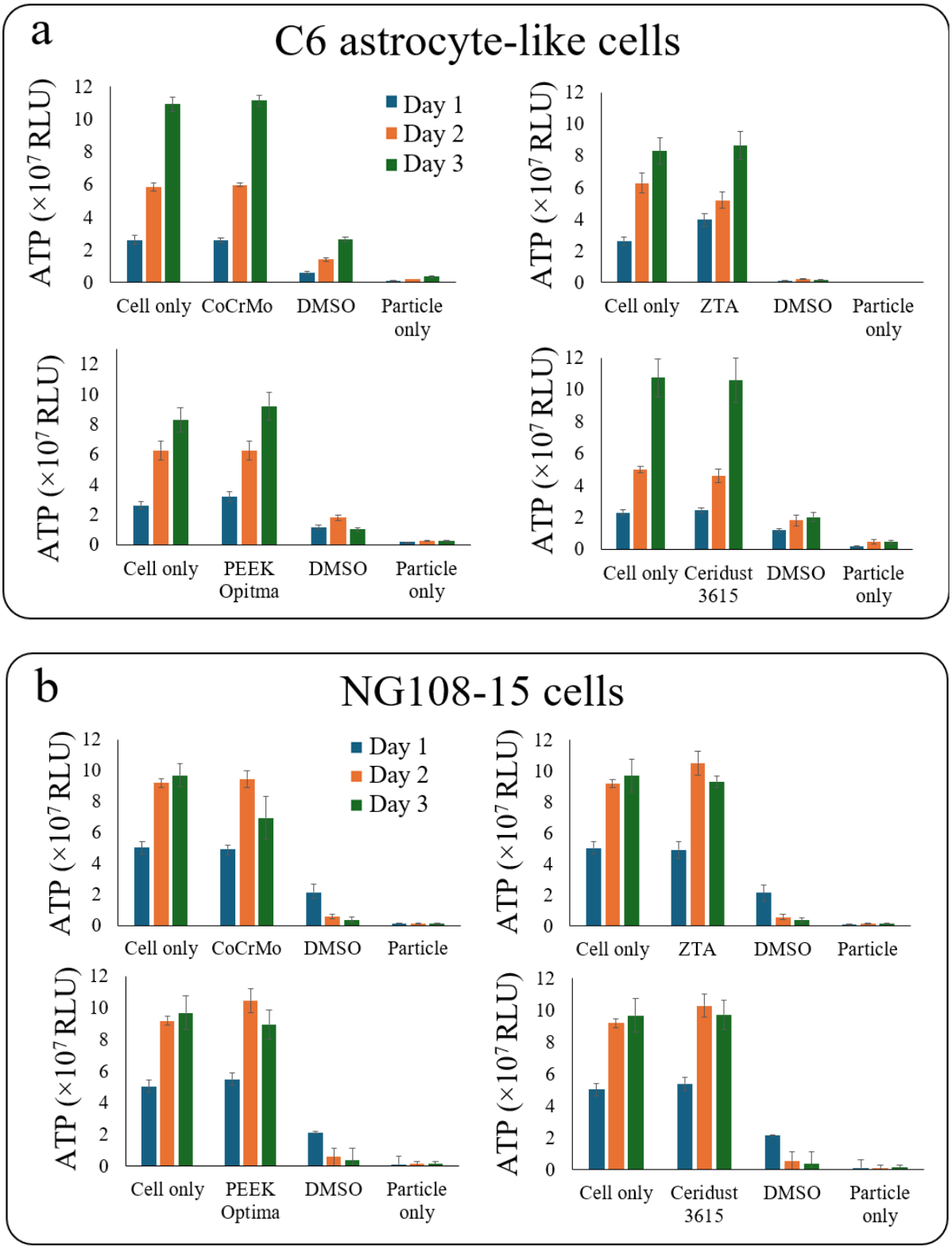

Figure 4. Cell viability comparison between the control sample (cell-only in 3D-bioprinted hydrogel) and CoCrMo, ZTA, PEEK-OPTIMA™, and Ceridust® 3615 model particles for C6 astrocyte-like (a) and NG108-15 cells (b). Abbreviations: CoCrMo: Cobalt–chromium–molybdenum; DMSO: Dimethyl sulfoxide; PEEK: Polyetheretherketone; ZTA: Zirconia-toughened alumina.

Table 2. Viability assessment of C6 astrocyte-like cells for various 3D model particles

Model particles	Culture time		
	Day 1	Day 3	Day 5
CoCrMo (0.5 μm³ per cell)	2.2 ± 0.09	6.0 ± 0.13	11.0 ± 0.24
CoCrMo (5 μm³ per cell)	2.7 ± 0.12	6.3 ± 0.21	11.0 ± 0.2
CoCrMo (50 μm³ per cell)	2.6 ± 0.17	6.0 ± 0.15	11.1 ± 0.66
PEEK-OPTIMA™	0.42 ± 0.06	0.72 ± 0.06	1.1 ± 0.09
Ceridust® 3615	0.25 ± 0.02	0.46 ± 0.04	1.0 ± 0.14
ZTA	0.39 ± 0.03	0.52 ± 0.02	0.52 ± 0.02

Notes: Data expressed as mean (±95% CI) luminescent values (×10⁶ RLU), determined by means of ATP assay.

Abbreviations: CoCrMo: Cobalt–chromium–molybdenum; PEEK: Polyetheretherketone; ZTA: Zirconia-toughened alumina.

Ceridust® 3615 and ZTA (p = 0.9). Notably, our post hoc analysis revealed a significant difference in cell viability between PEEK-OPTIMA™ and ZTA model particles (p = 0.021), where the cell viability was significantly lower after exposure to ZTA particles compared to PEEK-OPTIMA™ particles (Figure 5c).

Using the same approach, we also assessed the viability of NG108-15 cells. Our statistical analysis revealed a marginally significant interaction between culture time and biomaterial type (p < 0.051, Figure 5d). Both culture time and biomaterial type significantly influenced the viability of neuronal NG108-15 cells (p < 0.01; Figure 5e and f). Additionally, the post hoc analysis indicated that cell viability was significantly lower for CoCrMo compared to PEEK-OPTIMA™ (p = 0.007), Ceridust® 3615 (p = 0.002), and ZTA (p = 0.005) 3D model particles. No significant differences in the viability of NG108-15 cells were found between PEEK-OPTIMA™, Ceridust® 3615, and ZTA model particles (p < 0.71). Furthermore, the viability of NG108-15 cells varied significantly across culture time points (p < 0.001), with a progressive increase from Day 1 (5.2 ± 0.19) to Day 3 (10.1 ± 0.18), followed by a significant decrease on Day 5 (8.7 ± 0.18) (Figure 5e).

The proliferation of C6 astrocyte-like and NG108-15 cells across all 3D model particles was qualitatively evaluated (Figure 6) and compared to the negative control (C6 astrocyte-like cell-only 3D-bioprinted hydrogel). Qualitative assessment of cell viability, visualized using

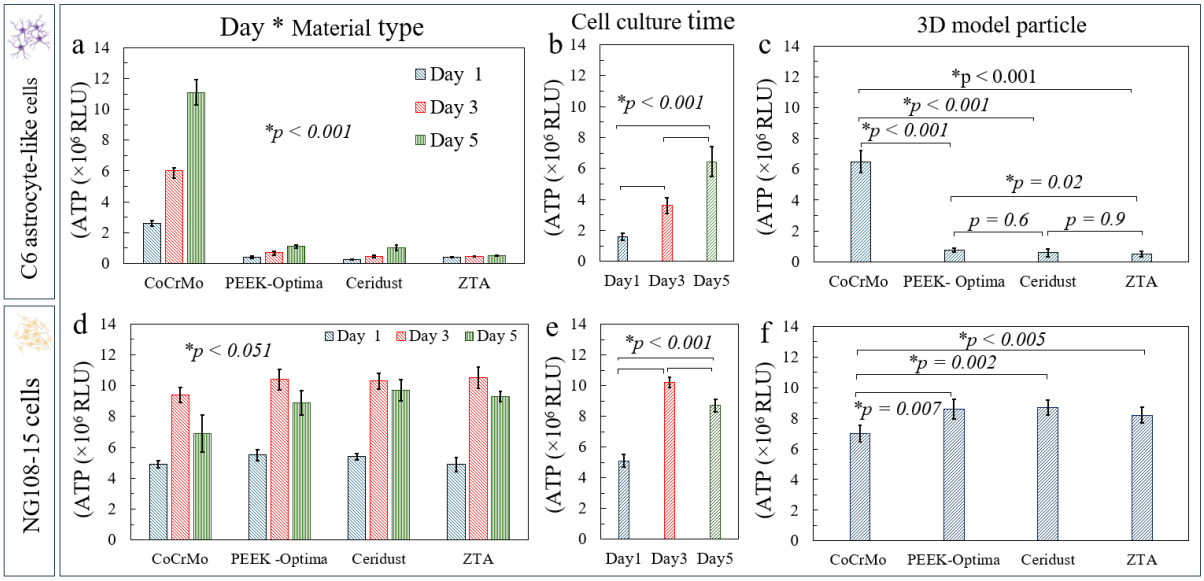

Figure 5. Estimated marginal means of cell viability, determined by means of ATP assay. (a, d) Interaction effects between culture duration and biomaterial type; (b, e) main effect of culture time; and (c, f) 3D model particles (material types) effects on the viability of C6 astrocyte-like cells (top) and NG108-15 cells (bottom). PEEK-OPTIMA™ and Ceridust® 3615 3D model particles were incorporated at a concentration of 100 μm³ per cell, whereas ZTA and CoCrMo model particles were introduced at 50 μm³ per cell. Abbreviations: CoCrMo: Cobalt–chromium–molybdenum; PEEK: Polyetheretherketone; ZTA: Zirconia-toughened alumina.

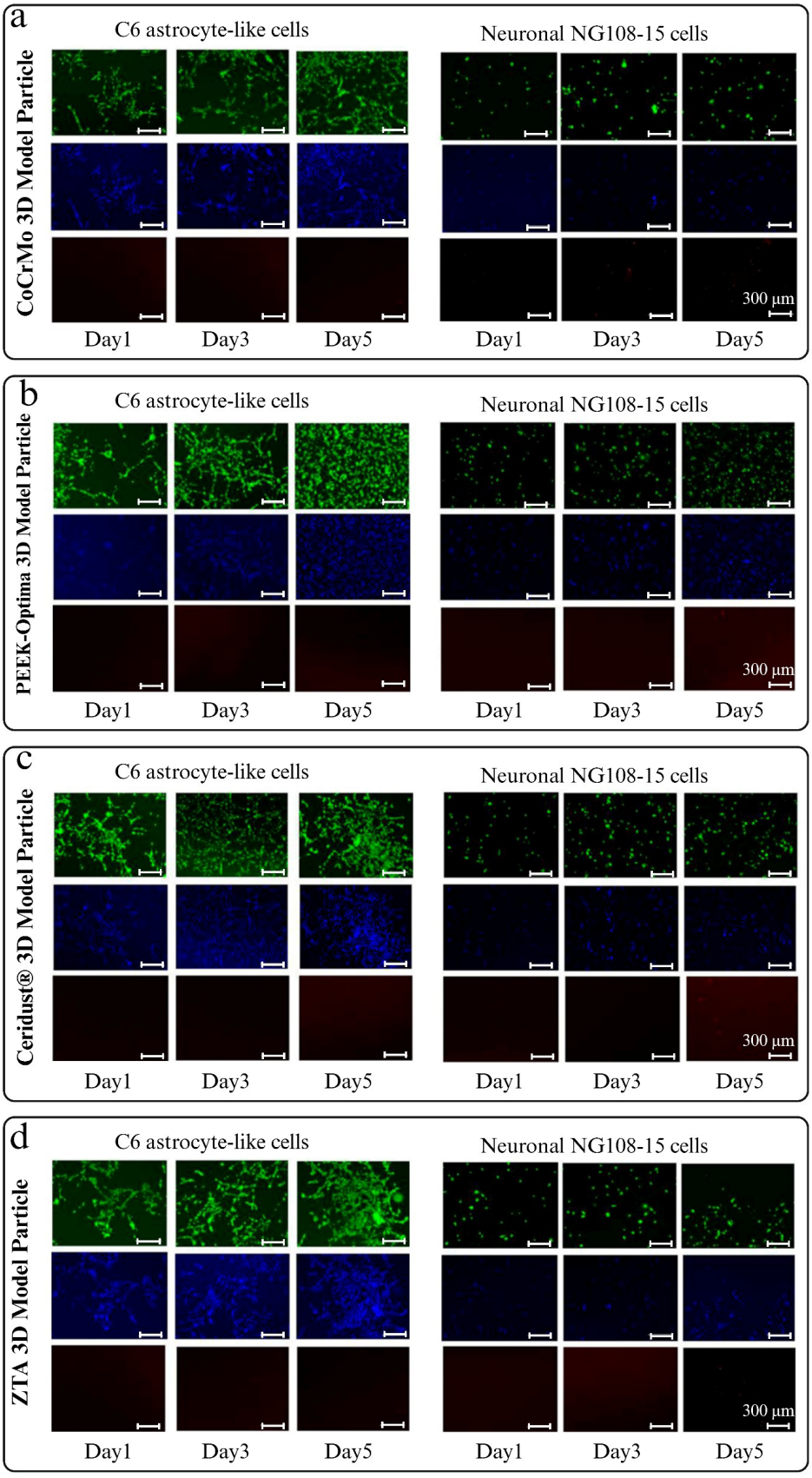
a
C6 astrocyte-like cells
Neuronal NG108-15 cells
CoCrMo 3D Model Particle
300 μm
Day1 Day3 Day5 Day1 Day3 Day5
b
C6 astrocyte-like cells
Neuronal NG108-15 cells
PEEK-Optima 3D Model Particle
300 μm
Day1 Day3 Day5 Day1 Day3 Day5
c
C6 astrocyte-like cells
Neuronal NG108-15 cells
Ceridust® 3D Model Particle
300 μm
Day1 Day3 Day5 Day1 Day3 Day5
d
C6 astrocyte-like cells
Neuronal NG108-15 cells
ZTA 3D Model Particle
300 μm
Day1 Day3 Day5 Day1 Day3 Day5

Figure 6. Qualitative analysis of the effect of CoCrMo (a), PEEK-OPTIMA™ (b), Ceridust® 3615 (c), and ZTA (d) model particles embedded in 3D-bioprinted GelMA on the viability of C6 astrocyte-like and NG108-15 cells (Days 1, 3, and 5). Live cells were stained with green-fluorescent calcein AM, cell nuclei with blue-fluorescent Hoechst, and dead cells with red-fluorescent propidium iodide. All scale bars = 300 μm. Abbreviations: CoCrMo: Cobalt–chromium– molybdenum; GelMA: Gelatin methacryloyl; PEEK: Polyetheretherketone; ZTA: Zirconia-toughened alumina.

live/dead fluorescence staining, supported the quantitative results. Live C6 astrocyte-like and NG108-15 cells were identified by green fluorescence (calcein AM), nuclei by blue fluorescence (Hoechst), and dead cells by red fluorescence (propidium iodide). Representative images from Days 1, 3, and 5 revealed cell viability patterns consistent with the luminescence-based measurements, confirming the material-dependent and time-dependent effects of CoCrMo, PEEK-OPTIMA™, Ceridust® 3615, and ZTA 3D model particles on both cell types.

3.3.2. Oxidative stress

The production of ROS by both C6 astrocyte-like and NG108-15 cells was assessed across all 3D model particles. Oxidative stress was measured on Days 3 and 5 using a DCFDA probe, where ROS production was directly proportional to the intensity of the green fluorescence. The estimated marginal mean (±95% CI) of fluorescent intensity, reflecting ROS production in C6 astrocyte-like and NG108-15 cells exposed to various model particles, is presented in Figure 7.

Statistical analysis revealed a significant interaction between culture duration and biomaterial type on ROS production in C6 astrocyte-like cells ($p = 0.003$; Figure 7a). Both the main effect of culture time ($p < 0.01$; Figure 7b) and the type of biomaterial used in the 3D model particles ($p = 0.032$; Figure 7c) were also statistically significant. Post hoc comparisons indicated that ROS production was markedly higher in cells exposed to CoCrMo particles compared to those exposed to PEEK-OPTIMA™ ($p = 0.007$), Ceridust® 3615 ($p = 0.025$), and ZTA ($p = 0.028$). No significant differences in ROS levels were observed among the PEEK-OPTIMA™, Ceridust® 3615, and ZTA groups ($p = 0.946$), suggesting a relatively comparable oxidative stress response among these materials.

Statistical analysis of ROS production by NG108-15 cells on Days 3 and 5 showed no significant interaction between culture duration and material type ($p = 0.34$; Figure 7d). Similarly, the main effect of culture time on ROS levels was not statistically significant ($p = 0.24$; Figure 7e). However, the type of biomaterial used in the 3D model particles had a significant overall effect on ROS production ($p = 0.04$; Figure 7f). Post hoc comparisons revealed that NG108-15 cells exposed to PEEK-OPTIMA™ particles produced significantly lower ROS compared to those exposed to CoCrMo ($p = 0.018$), Ceridust® 3615

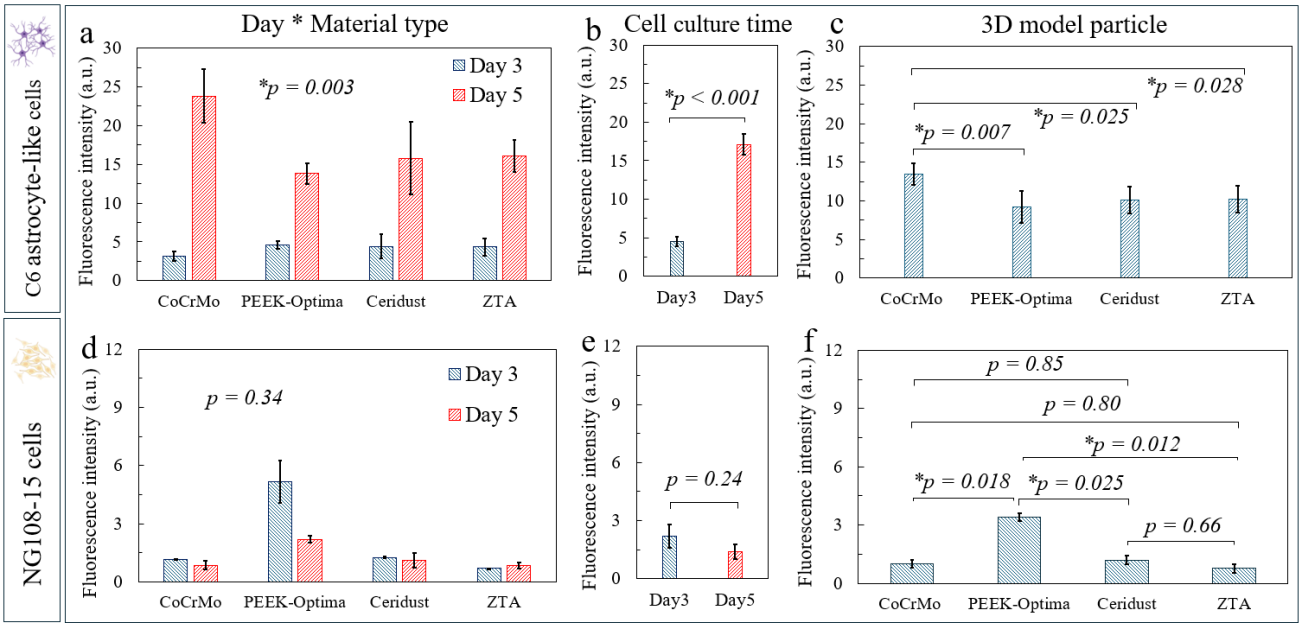

Figure 7. Reactive oxygen species (ROS) production by different cell types. (a, d) Effects of interaction between cell culture time and biomaterial type; (b, e) effects of culture time; and (c, f) effects of 3D model particles on the ROS production in C6 astrocyte-like (top) and NG108-15 cells (bottom). Abbreviations: CoCrMo: Cobalt–chromium–molybdenum; PEEK: Polyetheretherketone; ZTA: Zirconia-toughened alumina.

($p = 0.025$), and ZTA ($p = 0.012$). No significant differences in ROS levels were observed between CoCrMo and Ceridust® ($p = 0.85$), CoCrMo and ZTA ($p = 0.80$), or between Ceridust® 3615 and ZTA ($p = 0.66$). These findings suggest a relatively higher oxidative stress response in cells exposed to materials other than PEEK-OPTIMA™.

Quantitative analyses of C6 astrocyte-like cells showed that the positive control (cells with hydrogen peroxide) exhibited elevated ROS levels, as evidenced by the increased fluorescence intensity, compared to the cell-only negative control (Figure A1 in Appendix). The average fluorescence intensity of the positive control on Day 5 was significantly higher (approximately 70 times; $p < 0.05$) than that produced by all of the model particles (average fluorescence intensity < 22 ± 3.9 a.u.). Notably, all model particles did not induce significant ROS production compared to the cell-only negative control (average fluorescence intensity = 23.5 ± 5.4 a.u.). Similar results were observed for NG108-15 cells, where the positive control demonstrated higher ROS production (average fluorescence intensity = 37.1 ± 2.6 a.u.) than the cell-only negative control (average fluorescence intensity = 7.7 ± 5.8 a.u.) and any of the model particles (average fluorescence intensity < 2.1 ± 0.2 a.u.; $p < 0.05$) (**Figure S1, Supporting Information**). However, no significant increase in ROS production was detected in NG108-15 cells exposed to any of the model particles compared to the cell-only negative control.

The production of ROS by both C6 astrocyte-like and NG108-15 cells, embedded in 3D-bioprinted model particles, was qualitatively assessed using the DCFDA probe on Day 3. Production of ROS was proportional to the intensity of the green fluorescence (Figure 8a and b).

3.3.3. DNA integrity analysis

The DNA integrity of C6 astrocyte-like cells exposed to various model particles was assessed using a DNA damage assay that quantifies γ-H2AX foci as a marker of DNA strand breaks. DNA damage was evaluated at the 1-h mark, as genotoxic materials can induce immediate DNA strand breaks. Our findings revealed no detectable DNA damage in C6 astrocyte-like cells, as evidenced by the absence of γ-H2AX foci (Figure 8b).

4. Discussion

The primary objective of this study was to develop an advanced 3D spinal cord cellular model using bioprinting technology. While 3D bioprinting has been widely used in different biomedical studies,[36–38] this is the first study to engineer a 3D-bioprinted model that integrates neural cells with spinal implant wear particles and relevant biomaterials, establishing an advanced *in vitro* platform for evaluating the biological impact of wear debris. This novel approach offers a more physiologically relevant alternative to traditional 2D culture systems, enabling improved simulation of the *in vivo* microenvironment and more accurate assessment of cellular responses to biomaterial-associated particles.

We selected commercially available model particles derived from PEEK-OPTIMA™, Ceridust® 3615, ZTA ceramic, and CoCrMo alloy to represent a broad spectrum of biomaterials commonly used in spinal implant applications. This selection ensured comprehensive coverage of polymeric, ceramic, and metallic materials relevant to current clinical practice. Prior to embedding into neural cell-laden bioprinted GelMA hydrogels, the particles were thoroughly characterized for their size and morphology.

The SEM analysis of PEEK-OPTIMA™ model particles revealed irregular, granular morphologies. The particle size distribution showed a mode size between 0.1 and 0.8 μm, with an average diameter of 7.58 ± 3.97 μm. Notably, 95% of the particles were smaller than 8 μm. These results are consistent with those of Du et al.,[39] who reported that 99% of commercially available PEEK particles were under 5 μm, although their mean particle size was smaller (1.05 μm) compared to our findings. Furthermore, Hallab et al.[40] reported that PEEK-OPTIMA™ particles exhibited granular to flake-like morphologies, with 95% of the particles falling within the 1–10 μm size range, findings that are consistent with our current observations. The SEM analysis of Ceridust® 3615 particles revealed a predominantly granular morphology with noticeable agglomeration, aligning with observations reported by Liu et al.[35] In our study, the average particle size was 8.75 ± 2.35 μm following filtration through an 8 μm filter, and 5.27 ± 3.80 μm after passing through a 0.8 μm filter. These values are comparable to those reported by Green et al.,[41] who investigated murine peritoneal macrophage responses to polyethylene particles using Ceridust® 3615. Their work involved sequential filtration through 10, 1, 0.4, and 0.1 μm filters, resulting in particle sizes of 7.2 ± 3.15, 4.3 ± 1.89, 0.49 ± 0.11, and 0.21 ± 0.069 μm, respectively. ZTA particles in our study exhibited both granular and polygonal morphologies, with a size range of 0.1–0.8 μm and an average size of 3.69 ± 3.48 μm. These findings are consistent with those of Asif,[34] who also reported agglomerated structures of ZTA particles. In comparison, Germain et al.[42] investigated alumina powder and reported a smaller mean particle size of 0.5 ± 0.2 μm. The observed size discrepancy may be attributed to differences in particle generation and filtration techniques, as Germain et al. used a pin-on-plate wear simulator and employed finer filter membranes during particle separation.[42] The CoCrMo

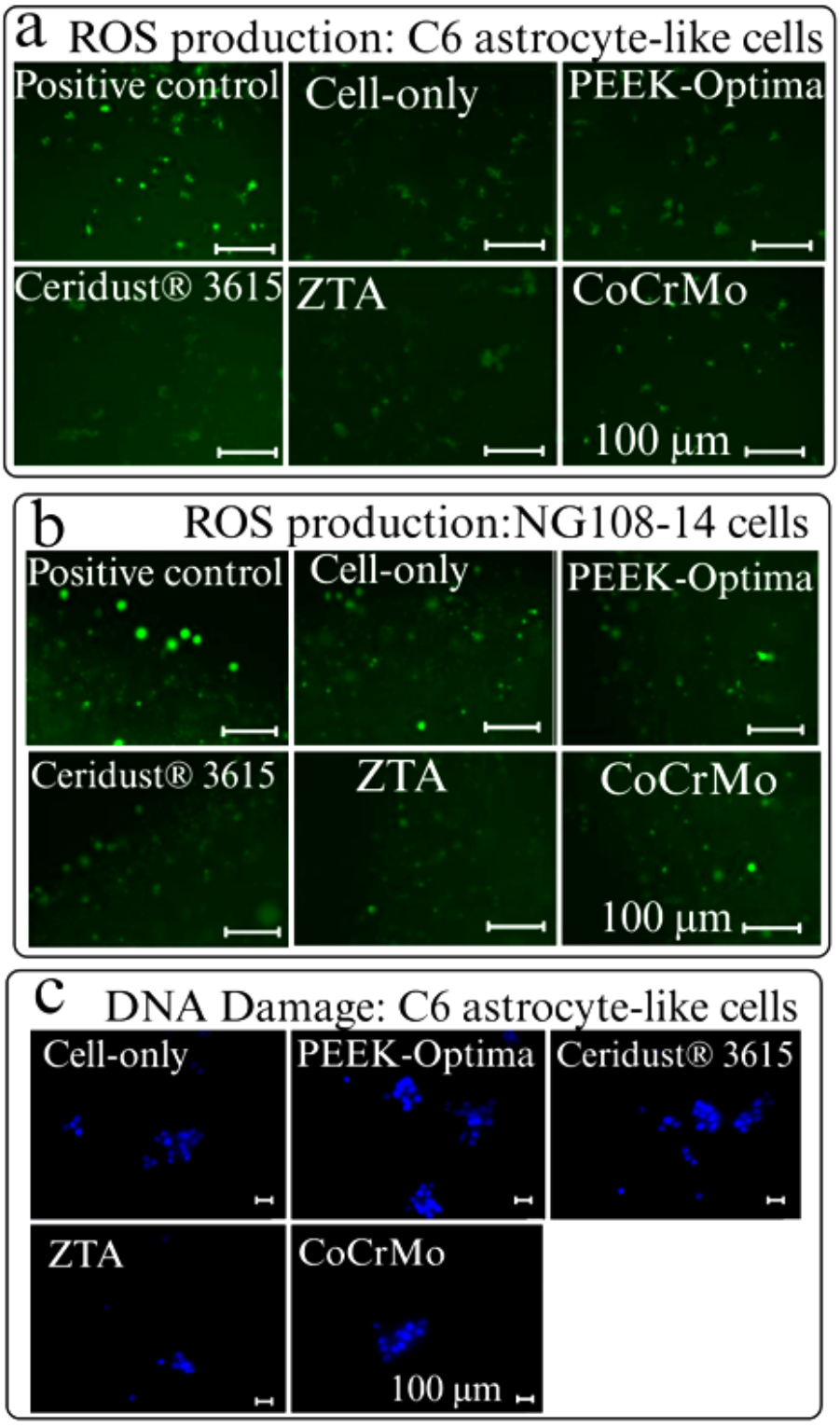

Figure 8. Fluorescence microscopy images showing ROS production in C6 astrocyte-like cells (a) and NG108-15 cells (b) embedded in 3D model particles after 3 days of culture. Oxidative stress was assessed using the DCFDA probe, which detects ROS activity. The intensity of green fluorescence correlates with ROS production. (c) DNA damage analysis via γ-H2AX immunofluorescence for C6 astrocyte-like cells exposed to different 3D model particles. Scale bars = 100 µm. Abbreviations: CoCrMo: Cobalt–chromium–molybdenum; PEEK: Polyetheretherketone; ROS: Reactive oxygen species; ZTA: Zirconia-toughened alumina.

particles predominantly exhibited a globular shape, with a mean size of 5.86 ± 1.20 μm, aligning with findings from Germain et al., who reported a mean size of 9.87 ± 5.67 μm for commercially available CoCr particles. However, when comparing these to clinically relevant CoCr particles generated via a pin-on-plate wear simulator, Germain et al.[42] and Lee et al.[26] observed aggregates and granular shapes, with some polygonal shards. Their reported mode size ranges for CoCr particles were 10–20 and 30–39 nm, respectively, while the mode size range in our study was 0.8–8 μm. This significant discrepancy in particle size may help explain the differences in biological responses observed in the current study.

In this study, bioprinting was used to create a 3D model incorporating neural cells and biomaterial particles for the first time. This platform offers significant advantages over traditional hydrogel casting methods, such as enhanced spatial precision for cellular placement and the ability to better replicate the *in vivo*-like organization of tissues.[43,44] By combining 5% (w/v) GelMA hydrogels and neural cells in bioprinted hydrogels, we established a promising 3D cell culture model for investigating neural cell responses to wear particles. The successful printing of model particles integrated with hydrogels and cells using extrusion-based bioprinting techniques demonstrated the potential of this approach. Printing parameters were adapted from previous studies, such as Rad et al.,[33] who successfully used GelMA hydrogels and neural cells in 3D-bioprinted constructs for spinal cord injury models. The temperature-sensitive properties of GelMA were key, as it undergoes reversible gelation with temperature change. Rad et al.[33] found that higher concentrations of GelMA (15% w/v) were needed at temperatures ≥32°C, while lower concentrations (2.5% w/v) were more effective at ≤22°C. Additionally, the current study confirmed that extrusion pressure was crucial for maintaining the structural integrity of GelMA constructs—too much pressure caused overflow, while insufficient pressure hindered extrusion. The nozzle size also played a critical role in successful extrusion, especially when printing hydrogels containing particles of metals, polymers, and ceramics. Smaller nozzles (25G, 0.25 mm; and 27G, 0.20 mm) were more likely to clog, whereas larger nozzles (20G, 0.58 mm; and 22G, 0.41 mm) enabled consistent, successful extrusion of cell-laden hydrogels with particles. Our results showed comparable growth and proliferation of cells in both 2D- and 3D-bioprinted cultures over 7 days. These findings were consistent with Rad et al.,[33] who reported similar results using 5% (w/v) GelMA hydrogel for the same cell lines.

In this study, C6 astrocyte-like and NG108-15 cells were exposed to model particles, with PEEK-OPTIMA™ and Ceridust® 3615 particles administered at a concentration of 100 μm³ per cell, and ZTA and CoCrMo particles at 50 μm³ per cell. In all model particle groups, 95% of the particles ranged from 0.1 to 8 μm in size. We assessed cell viability, ROS production, and DNA damage over 7 days to capture both immediate and cumulative cellular responses to model particles. Initial testing of CoCrMo particles at concentrations of 0.5, 5, and 50 μm³ per cell showed no significant differences in biological responses, prompting the selection of 50 μm³ per cell for further testing. No significant changes in cell viability or ROS production were observed between the cell-only controls and model particle groups for both cell types, likely due to the short culture duration. However, the study revealed significant variations in cell viability and ROS production, which were influenced by culture time, biomaterial type, and the interactions between particles and cells.

The literature on neural cell responses to different model particles, particularly in studies comparing the biological impact of various particles using 3D *in vitro* models, remains limited. One notable study by Hallab et al.[40] investigated macrophage reactivity to PEEK-OPTIMA™ particles versus ultra-high-molecular-weight polyethylene (UHMWPE) particles, using differentiated human macrophages and primary human monocytes. They found that PEEK-OPTIMA™ particles (0.7 and 2.4 μm) did not significantly affect cell viability after 24 or 48 h.[40] This finding is especially relevant, as our study is the first to examine neural cell responses to PEEK-OPTIMA™ particles *in vitro*. Hallab et al.[40] also reported that PEEK-OPTIMA™ particles induced significant increases in proinflammatory cytokine levels compared to the control, though their inflammatory response was less pronounced than that of UHMWPE particles. Although our current study did not focus on inflammation, future research should investigate the impact of PEEK-OPTIMA™ particles on cytokine production in neural cells. Additionally, Hallab et al.[45] conducted an *in vivo* study using a rabbit model to explore the effects of PEEK-OPTIMA™ particles via epidural and intradiscal injections, which resulted in neurological damage. This highlights the critical need to understand the biological effects of PEEK-OPTIMA™ particles on neural cells and tissues.[30,45,46] In line with these findings, our study observed no major negative impact on cell viability, with similar results between the cell-only and 3D model particle groups. However, a noteworthy observation was the significantly higher production of ROS by NG108-15 cells exposed to PEEK-OPTIMA™ particles. This increase in ROS production warrants further investigation into the potential long-term effects of PEEK-OPTIMA™ particles in spinal environments. Understanding how PEEK-OPTIMA™ interacts with neural tissues is essential for evaluating its safety and clinical outcomes. Such knowledge

is critical for guiding clinicians and patients in the use of PEEK-OPTIMA™ in spinal implants, as the interactions with neural cells may influence the implants' long-term success and health implications.

Previous studies have explored the biological responses to Ceridust® 3615 particles using *in vitro* gel encapsulation techniques. Green et al.[41] encapsulated Ceridust® 3615 particles in 1% (w/v) agarose gel, then centrifuged the mixture to create a monolayer of particles. Murine peritoneal macrophages were seeded on top, and after 24 h, no significant impact on cell viability was observed at a 100 μm³ per cell concentration compared to the cell-only control. This technique was later adapted by Liu et al.,[35] who used a 0.4% (w/v) agarose gel without centrifugation, enhancing the gel's porosity and dispersing the particles more widely. They also replaced murine macrophages with human peripheral blood mononuclear cells and found similar results, with no significant effect on cell viability after 24 h. Further supporting these findings, Yarrow-Wright's study[47] confirmed that the Ceridust® 3615 particles did not adversely affect the viability of either human peripheral blood mononuclear cells or murine peritoneal macrophages in agarose and collagen gels. However, no studies have yet investigated the response of neural cells to Ceridust® 3615 particles *in vitro*. This gap highlights the need for further research into how Ceridust® 3615 interacts with neural cells, especially within 3D *in vitro* models. The current study used GelMA hydrogels to culture C6 astrocyte-like and NG108-15 cells, following the method of Rad et al.,[33] who demonstrated cell viability over 7 days. The particle size of Ceridust® 3615 (>99%) aligned with that reported by Green et al.[41] Consistent with prior findings, no significant reduction in cell viability, ROS production, or DNA damage was observed in either cell type exposed to Ceridust® 3615 particles. The lack of adverse effects may be due to the particle size, as larger particles are less likely to be internalized by cells.[41] Future studies should investigate the impact of clinically relevant particle sizes on neural cell responses. Additionally, studies by Hallab et al.[40] and Liu et al.[35] found no significant release of osteolytic cytokines from cells exposed to Ceridust® 3615. Future research should explore its impact on neural cell inflammatory responses, offering further insights for clinical applications.

The biological impact of BIOLOX Delta ZTA wear particles has been investigated in studies involving fibroblasts and peripheral blood mononuclear cells, with Asif[34] reporting minimal biological effects and suggesting potential improvements in long-term clinical performance. Although ZTA is used in spinal cages, concerns about the brittleness of ZTA under certain loading conditions continue to limit its use in spinal implants, as fractures can occur under excessive mechanical forces.[48] In the current study, neural cells were exposed to ZTA model particles at a dosage of 50 μm³, and cell viability was assessed over 5 days. No significant changes in cell viability were observed in either C6 astrocyte-like or NG108-15 cells, compared to the cell-only negative control. Interestingly, significantly lower ROS production was observed in the 3D ZTA model compared to other particle types. Although previous research has not explored neural cell responses to ZTA particles, similar studies on other cell types, such as L929 fibroblasts, have reported comparable findings. Germain et al.[42] observed no significant reduction in cell viability when fibroblasts were exposed to commercially available ceramic powders but noted cytotoxic effects when U937 human macrophages were exposed to clinically relevant ceramic wear particles at a dose of 50 μm³ per cell. The lack of cytotoxicity observed in our study with neural cells aligns with the findings in fibroblasts. Additionally, Asif[34] reported no adverse effects on L929 cell viability when exposed to BIOLOX Delta ceramic particles at a similar dosage. Furthermore, ZTA particles in our study did not induce ROS production or DNA damage in either C6 astrocyte-like or NG108-15 cells, reinforcing the conclusion that ZTA particles are biologically inert in neural cell cultures. These results are consistent with those of Asif,[34] who found no significant oxidative stress or DNA damage in peripheral blood mononuclear cells exposed to ceramic particles. However, their study also revealed that clinically relevant ceramic wear particles at the same dosage did induce DNA damage, highlighting differences in biological effects between model particles and clinically relevant materials. Future studies should focus on using clinically relevant ceramic wear particles at the same dosage (50 μm³ per cell) to determine if the cytotoxic effects observed in fibroblasts extend to neural cells. This approach will provide a clearer understanding of the potential biological risks associated with ceramic-based spinal implants in a clinically relevant context.

Prior research by Lee et al. utilized Type I rat tail collagen gel to examine the responses of primary astrocytes and microglia to CoCrMo wear particles at doses ranging from 0.5 to 50 μm³ per cell over 5 days.[26] Their findings revealed a significant reduction in astrocyte viability at the highest dose (50 μm³) after 2 and 5 days. However, the use of collagen hydrogels introduced limitations, such as poor structural integrity and batch-to-batch variability, which could affect the results. In contrast, the current study demonstrated that C6 astrocyte-like cells maintained viability across all CoCrMo particle doses (0.5–50 μm³ per cell) over the same exposure period. A notable reduction in NG108-15 cell viability was observed only at the highest dose (50 μm³) after 5 days, compared to the cell-only

negative control. These findings suggest that the 3D model used in this study offers improved stability and reliability, allowing for a more accurate evaluation of neural cell responses to CoCrMo particles. The distinct responses of C6 astrocyte-like and NG108-15 cells to CoCrMo particles likely stem from their differing sensitivities to foreign materials. Astrocytes, known for their structural support and role in tissue repair within the central nervous system, exhibit greater resilience to such exposure. In contrast, the more sensitive NG108-15 cells are less equipped to tolerate foreign materials. These findings highlight the need for further research to understand the cellular mechanisms behind these responses, which is essential for improving the safety and effectiveness of spinal implants and minimizing neural tissue damage. No significant oxidative stress or DNA damage was detected in C6 astrocyte-like or NG108-15 cells following 24 h of exposure to model CoCrMo particles. This contrasts with findings by Lee et al.,[26] who reported significant DNA damage in primary astrocytes under similar conditions. The discrepancy may stem from differences in cell models, particle characteristics, or experimental conditions, underscoring the need for further research to clarify the varying cellular responses to CoCrMo particles. The discrepancies between this study and Lee et al.'s investigation can be attributed to key differences in the experimental models, particularly the type and size of CoCrMo particles used.

In the current study, we developed a novel 3D-bioprinted spinal cord model integrating neural cells with spinal implant wear particles and biomaterials, establishing the first *in vitro* platform of its kind to assess the biological effects of wear debris. While the 3D constructs in this study were deposited in droplet format, the use of a bioprinter was essential for ensuring precise and reproducible placement, volumetric consistency, and homogeneous distribution of cells and particles across replicates. Unlike manual pipetting, the bioprinter allowed for controlled deposition of defined volumes and bioink compositions, which is critical when evaluating cellular responses to different biomaterial particles. Additionally, bioprinting supports future scalability and integration into more complex architectures, which aligns with our longer-term aim of developing advanced neural tissue models. Compared to traditional casting, bioprinting offers superior control over the distribution and organization of cells and particles within hydrogels.[49] In casting, sedimentation and uneven mixing often lead to heterogeneous distribution, whereas bioprinting ensures uniform dispersion by precisely depositing cell-particle-laden hydrogels. Bioprinting also applies minimal and consistent mechanical stress on cells during fabrication, reducing unintended shear forces common in casting or manual handling.[50] Additionally, gelation can be finely controlled in bioprinting through synchronized light exposure or temperature regulation, leading to reproducible and structurally stable constructs. This controlled environment results in higher fidelity in model architecture and better mimics the native tissue microenvironment. Despite the valuable insights gained, one of the limitations of the current study was the use of commercially available model particles, not clinically representative wear-simulated particles, particularly in terms of size, morphology, and chemical composition. As these particles differ from those typically generated in clinical settings, future studies should aim to replicate these experiments with clinically relevant particles to better understand neural cell responses *in vitro* within the same 3D-bioprinted GelMA hydrogel model. Moreover, examining the cumulative or synergistic effects of multiple biomaterial wear particles, such as those from metals, ceramics, and polymers, could provide deeper insights into the overall impact on neural tissue, particularly in the context of multi-material spinal implants. Expanding the scope in these areas will enhance the clinical relevance of the findings and support the development of safer, more effective biomaterials for spinal and neural tissue applications. While no significant difference in cell viability was observed between the 2D and 3D cultures, this is a positive outcome, as cell viability often decreases in 3D systems due to limited nutrient diffusion. The ability of our 3D-bioprinted model to maintain comparable viability suggests good biocompatibility and supports its use for further physiological studies. Future work will focus on evaluating neural-specific functions and comparing cell behavior in this model to native tissue to further validate its physiological relevance. Another limitation of this study was the use of cell lines (C6 and NG108-15), which do not fully represent the functionality and cellular heterogeneity of the spinal cord, particularly due to the absence of microglia. These cell lines were chosen to establish a robust and reproducible 3D-bioprinted model and to assess the feasibility of incorporating spinal implant biomaterial-derived particles in the 3D-bioprinted system. Future work should focus on incorporating primary or induced pluripotent stem cell (iPSC)-derived neural cells, including microglia, to enhance the physiological relevance of the model.

5. Conclusion

This study established a 3D-bioprinted spinal cord cellular model that integrates neural cells with spinal implant wear particles. It represents the first *in vitro* platform designed to investigate the biological effects of wear debris in a physiologically relevant context. By incorporating model particles with diverse morphologies (ranging from irregular to spherical), sourced from different biomaterials, and

administering them in a 3D-bioprinted GelMA hydrogel, we enabled precise and reproducible evaluation of particle–cell interactions. Short-term exposure did not significantly impact cell viability or ROS production across the tested conditions. However, our results revealed significant variations in cell viability and ROS production, which were influenced by culture time, biomaterial type, and the interactions between particles and cells. In particular, CoCrMo particles had a greater impact on cell viability compared to the other biomaterials tested. These findings underscore the potential of this bioprinted platform as a powerful tool for future long-term mechanistic studies and preclinical assessments of spinal implant biocompatibility.

Acknowledgments

None.

Funding

None.

Conflict of interest

The authors declare they have no competing interests

Author contributions

Conceptualization: Joanne L. Tipper
Formal analysis: Joanne L. Tipper, David J. Wen, Javad Tavakoli
Investigation: David J. Wen
Methodology: Joanne L. Tipper, David J. Wen, Javad Tavakoli
Writing–original draft: Javad Tavakoli, David J. Wen
Writing–review & editing: Joanne L. Tipper, Javad Tavakoli

Ethics approval and consent to participate

Not applicable.

Consent for publication

Not applicable.

Availability of data

Data is available from the corresponding author upon reasonable request.

References

1. Tavakoli J, Diwan AD, Tipper JL. Advanced strategies for the regeneration of lumbar disc annulus fibrosus. *Int J Mol Sci*. 2020;21(14):4889.
doi: 10.3390/ijms21144889

2. Wen DJ, Tavakoli J, Tipper JL. Lumbar total disc replacements for degenerative disc disease: a systematic review of outcomes with a minimum of 5 years follow-up. *Global Spine J*. 2024;14(6):1827-1837.
doi: 10.1177/21925682241228756

3. Zeegers W, Bohnen L, Laaper M, Verhaegen M. Artificial disc replacement with the modular type SB Charite III: 2-year results in 50 prospectively studied patients. *Eur Spine J*. 1999;8:210-217.
doi: 10.1007/s005860050160

4. Vicars R, Hyde PJ, Brown TD, et al. The effect of anterior–posterior shear load on the wear of ProDisc-L TDR. *Eur Spine J*. 2010;19(8):1356-1362.
doi: 10.1007/s00586-010-1396-8

5. Vicars R, Prokopovich P, Brown TD, et al. The effect of anterior-posterior shear on the wear of CHARITÉ total disc replacement. *Spine (Phila Pa 1976)*. 2012;37(9):E528-E534.
doi: 10.1097/BRS.0b013e31823cbd6e

6. Hallab NJ. A review of the biologic effects of spine implant debris: fact from fiction. *SAS J*. 2009;3(4):143-160.
doi: 10.1016/j.esas.2009.11.005

7. Chang B-S, Brown PR, Sieber A, Valdevit A, Tateno K, Kostuik JP. Evaluation of the biological response of wear debris. *Spine J*. 2004;4(6):S239-S244.
doi: 10.1016/j.spinee.2004.07.014

8. Ganko R, Madhavan A, Hamouda W, et al. Spinal implant wear particles: generation, characterization, biological impacts, and future considerations. *iScience*. 2025;28(4):112193.
doi: 10.1016/j.isci.2025.112193

9. Punt IM, Austen S, Cleutjens JP, et al. Are periprosthetic tissue reactions observed after revision of total disc replacement comparable to the reactions observed after total hip or knee revision surgery? *Spine (Phila Pa 1976)*. 2012;37(2):150-159.
doi: 10.1097/brs.0b013e3182154c22

10. San-Juan R, Paredes I, Ramírez-Nava E, et al. Reduction of instrumentation-related spine surgical site infections after optimization of surgical techniques. a single center retrospective analysis. *Global Spine J*. 2024;14(2):438-446.
doi: 10.1177/21925682221109557

11. Xu R, Ebraheim NA, Nadaud MC, Phillips ER. Local tissue of the lumbar spine response to titanium plate-screw system. *Spine (Phila Pa 1976)*. 1996;21(7):871-873.
doi: 10.1097/00007632-199604010-00020

12. Lin T-h, Tamaki Y, Pajarinen J, et al. Chronic inflammation in biomaterial-induced periprosthetic osteolysis: NF-κB as a therapeutic target. *Acta Biomater*. 2014;10(1):1-10.
doi: 10.1016/j.actbio.2013.09.034

13. Zairi F, Remacle JM, Allaoui M, Assaker R. Delayed hypersensitivity reaction caused by metal-on-metal total disc replacement: case report. *J Neurosurg Spine*. 2013;19(3):389-391.
doi: 10.3171/2013.6.spine121010

14. Zeh A, Planert M, Siegert G, Lattke P, Held A, Hein W. Release of cobalt and chromium ions into the serum following implantation of the metal-on-metal Maverick-type artificial lumbar disc (Medtronic Sofamor Danek). *Spine (Phila Pa 1976)*. 2007;32(3):348-352. doi: 10.1097/01.brs.0000253599.89694.c0

15. AlZeedi M, Al Rawahi S, Muwanis M, Alraiyes TM, Al Farii H, Jarzem P. Pseudotumor after total disc replacement in the lumbar spine: a case report and review of the literature. *N Am Spine Soc J*. 2022;9:100107. doi: 10.1016/j.xnsj.2022.100107

16. Tavakoli J, Hu Q, Tipper JL, Tang Y. Aggregation-induced emission biomarkers for early detection of orthopaedic implant failure. *Aggregate*. 2024;5(6):e645. doi: 10.1002/agt2.645

17. Austen S, Punt IM, Cleutjens JP, et al. Clinical, radiological, histological and retrieval findings of Activ-L and Mobidisc total disc replacements: a study of two patients. *Eur Spine J*. 2012;21:513-520. doi: 10.1007/s00586-011-2141-7

18. Yang G, Gu M, Chen W, et al. SPHK-2 promotes the particle-induced inflammation of RAW264.7 by maintaining consistent expression of TNF-α and IL-6. *Inflammation*. 2018;41(4):1498-1507. doi: 10.1007/s10753-018-0795-6

19. Yoshitake F, Itoh S, Narita H, Ishihara K, Ebisu S. Interleukin-6 directly inhibits osteoclast differentiation by suppressing receptor activator of NF-kappaB signaling pathways. *J Biol Chem*. 2008;283(17):11535-11540. doi: 10.1074/jbc.m607999200

20. Ayers R, Miller M, Schowinsky J, Burger E, Patel V, Kleck C. Three cases of metallosis associated with spine instrumentation. *J Mater Sci Mater Med*. 2017;29(1):3. doi: 10.1007/s10856-017-6011-7

21. Punt IM, Cleutjens JPM, de Bruin T, et al. Periprosthetic tissue reactions observed at revision of total intervertebral disc arthroplasty. *Biomaterials*. 2009;30(11):2079-2084. doi: 10.1016/j.biomaterials.2008.12.071

22. Cunningham BW, Orbegoso CM, Dmitriev AE, et al. The effect of spinal instrumentation particulate wear debris: an in vivo rabbit model and applied clinical study of retrieved instrumentation cases. *Spine J*. 2003;3(1):19-32. doi: 10.1016/S1529-9430(02)00443-6

23. Lin T-h, Yao Z, Sato T, et al. Suppression of wear-particle-induced pro-inflammatory cytokine and chemokine production in macrophages via NF-κB decoy oligodeoxynucleotide: a preliminary report. *Acta Biomater*. 2014;10(8):3747-3755. doi: 10.1016/j.actbio.2014.04.034

24. Luo G, Li Z, Wang Y, et al. Resveratrol protects against titanium particle-induced aseptic loosening through reduction of oxidative stress and inactivation of NF-κB. *Inflammation*. 2016;39(2):775-785. doi: 10.1007/s10753-016-0306-6

25. Hallab NJ, Cunningham BW, Jacobs JJ. Spinal implant debris-induced osteolysis. *Spine (Phila Pa 1976)*. 2003;28(20S):S125-S138. doi: 10.1097/00007632-200310151-00006

26. Lee H, Phillips JB, Hall RM, Tipper JL. Neural cell responses to wear debris from metal-on-metal total disc replacements. *Eur Spine J*. 2020;29(11):2701-2712. doi: 10.1007/s00586-019-06177-w

27. Papageorgiou I, Marsh R, Tipper JL, Hall RM, Fisher J, Ingham E. Interaction of micron and nano-sized particles with cells of the dura mater. *J Biomed Mater Res B Appl Biomater*. 2014;102(7):1496-1505. doi: 10.1002/jbm.b.33129

28. Behl B, Papageorgiou I, Brown C, et al. Biological effects of cobalt-chromium nanoparticles and ions on dural fibroblasts and dural epithelial cells. *Biomaterials*. 2013;34(14):3547-3558. doi: 10.1016/j.biomaterials.2013.01.023

29. Papageorgiou I, Abberton T, Fuller M, Tipper JL, Fisher J, Ingham E. Biological effects of clinically relevant cocr nanoparticles in the dura mater: an organ culture study. *Nanomaterials*. 2014;4(2):485-504. doi: 10.3390/nano4020485

30. Cunningham BW, Hallab NJ, Hu N, McAfee PC. Epidural application of spinal instrumentation particulate wear debris: a comprehensive evaluation of neurotoxicity using an in vivo animal model. *J Neurosurg Spine*. 2013;19(3):336-350. doi: 10.3171/2013.5.spine13166

31. Stoodley MA, Jones NR, Brown CJ. Evidence for rapid fluid flow from the subarachnoid space into the spinal cord central canal in the rat. *Brain Res*. 1996;707(2):155-164. doi: 10.1016/0006-8993(95)01228-1

32. Stoodley MA, Brown SA, Brown CJ, Jones NR. Arterial pulsation-dependent perivascular cerebrospinal fluid flow into the central canal in the sheep spinal cord. *J Neurosurg*. 1997;86(4):686-693. doi: 10.3171/jns.1997.86.4.0686

33. Rad MA, Mahmodi H, Filipe EC, Cox TR, Kabakova I, Tipper JL. Micromechanical characterisation of 3D bioprinted neural cell models using Brillouin microspectroscopy. *Bioprinting*. 2022;25:e00179. doi: 10.1016/j.bprint.2021.e00179

34. Asif IM. *Characterisation and Biological Impact of Wear Particles from Composite Ceramic Hip Replacements*. University of Leeds; 2018. https://etheses.whiterose.ac.uk/id/oai_id/oai:etheses.whiterose.ac.uk:20563

35. Liu A, Richards L, Bladen CL, Ingham E, Fisher J, Tipper JL. The biological response to nanometre-sized polymer particles. *Acta Biomater*. 2015;23:38-51. doi: 10.1016/j.actbio.2015.05.016

36. Kim A, Mo K, Choe S, Shin M, Yoon H. Comprehensive insight into 3D bioprinting technology for brain tumor modelling. *IJB*. 2024;10(6):4166.
doi: 10.36922/ijb.4166

37. Tang H, Zhao E, Lai Y, et al. 3D bioprinting techniques and hydrogels for osteochondral integration regeneration. *IJB*. 2024;10(6):4472.
doi: 10.36922/ijb.4472

38. Hou Y-C, Cui X, Qin Z, et al. Three-dimensional bioprinting of artificial blood vessel: process, bioinks, and challenges. *IJB*. 2023;9(4):740.
doi: 10.18063/ijb.740

39. Du Z, Zhu Z, Wang Y. The degree of peri-implant osteolysis induced by PEEK, CoCrMo, and HXLPE wear particles: a study based on a porous Ti6Al4V implant in a rabbit model. *J Orthop Surg Res*. 2018;13(1):23.
doi: 10.1186/s13018-018-0736-y

40. Hallab NJ, McAllister K, Brady M, Jarman-Smith M. Macrophage reactivity to different polymers demonstrates particle size- and material-specific reactivity: PEEK-OPTIMA® particles versus UHMWPE particles in the submicron, micron, and 10 micron size ranges. *J Biomed Mater Res B Appl Biomater*. 2012;100B(2):480-492.
doi: 10.1002/jbm.b.31974

41. Green TR, Fisher J, Stone M, Wroblewski BM, Ingham E. Polyethylene particles of a 'critical size' are necessary for the induction of cytokines by macrophages in vitro. *Biomaterials*. 1998;19(24):2297-2302.
doi: 10.1016/s0142-9612(98)00140-9

42. Germain M, Hatton A, Williams S, et al. Comparison of the cytotoxicity of clinically relevant cobalt–chromium and alumina ceramic wear particles in vitro. *Biomaterials*. 2003;24(3):469-479.
doi: 10.1016/s0142-9612(02)00360-5

43. Bishop ES, Mostafa S, Pakvasa M, et al. 3-D bioprinting technologies in tissue engineering and regenerative medicine: Current and future trends. *Genes Dis*. 2017;4(4):185-195.
doi: 10.1016/j.gendis.2017.10.002

44. Yu J, Park SA, Kim WD, et al. Current advances in 3D bioprinting technology and its applications for tissue engineering. *Polymers*. 2020;12(12):2958.
doi: 10.3390/polym12122958

45. Hallab NJ, Bao Q-B, Brown T. Assessment of epidural versus intradiscal biocompatibility of PEEK implant debris: an in vivo rabbit model. *Eur Spine J*. 2013;22:2740-2751.
doi: 10.1007/s00586-013-2904-4

46. Stratton-Powell AA, Pasko KM, Brockett CL, Tipper JL. The biologic response to polyetheretherketone (PEEK) wear particles in total joint replacement: a systematic review. *Clin Orthop Relat Res*. 2016;474(11):2394-2404.
doi: 10.1007/s11999-016-4976-z

47. Yarrow-Wright LE. *Development of a Novel 3D In Vitro Model to Measure Cellular Response to Antioxidant Doped Highly Cross-Linked Ultra High Molecular Weight Polyethylene Wear Debris*. University of Leeds; 2018.
https://etheses.whiterose.ac.uk/id/oai_id/oai:etheses.whiterose.ac.uk:24128

48. Kölle L, Ignasiak D, Ferguson SJ, Helgason B. Ceramics in total disc replacements: a scoping review. *Clin Biomech*. 2022;100:105796.
doi: 10.1016/j.clinbiomech.2022.105796

49. Jaksa L, Aryeetey OJ, Hatamikia S, et al. 3D-printed multi-material liver model with simultaneous mechanical and radiological tissue-mimicking features for improved realism. *IJB*. 2023;9(4):721.
doi: 10.18063/ijb.721

50. Yuk JC, Nam KH, Park SH. Additive-manufactured synthetic bone model with biomimicking tunable mechanical properties for evaluation of medical implants. *IJB*. 2024;10(1):1067.
doi: 10.36922/ijb.1067

Appendix

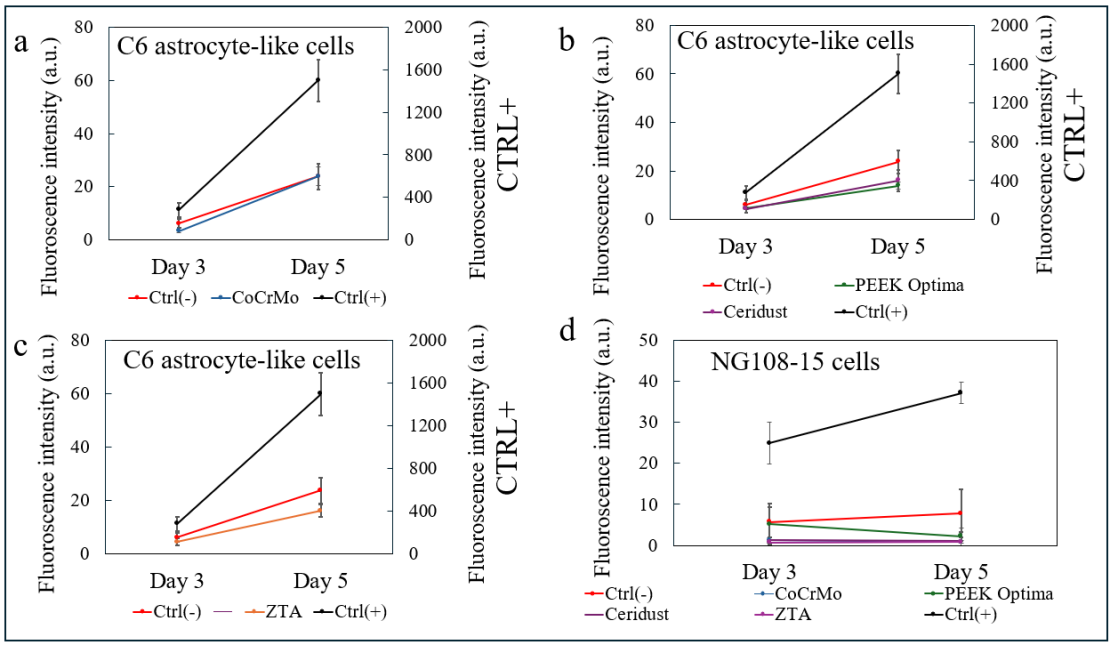

Figure A1. Comparison of ROS production by C6 astrocyte-like cells between controls (negative: cell-only; and positive: cell-H_2O_2) and 3D model particles: (a) CoCrMo, (b) PEEK-OPTIMA™ and Ceridust®, and (c) ZTA. (d) Comparison of ROS production by NG108-15 cells between controls (negative: cell-only; and positive: cell-H_2O_2) and all 3D model particles. Abbreviations: CoCrMo: Cobalt–chromium–molybdenum; PEEK: Polyetheretherketone; ROS: Reactive oxygen species; ZTA: Zirconia-toughened alumina.